JOURNAL OF MAGNETIC RESONANCE **124,** 298–309 (1997)
ARTICLE NO. MN961034

# Conformational Equilibria in Polypeptides. I. Determination of Accurate $^3J_{HC}$ Coupling Constants in Antamanide by 2D NMR Multiplet Simulation

JÜRGEN M. SCHMIDT

*Institut für Biophysikalische Chemie, Johann Wolfgang Goethe-Universität, Biozentrum N230, Marie-Curie-Strasse 9, D-60439 Frankfurt am Main, Germany*

Received April 11, 1996; revised October 11, 1996

**High-precision heteronuclear three-bond coupling constants including $^3J(H^N, C')$, $^3J(H^N, C^\beta)$, $^3J(H^\alpha, C^\gamma)$, and $^3J(H^\beta, C')$ are determined for the nonproline residues in uniformly $^{13}C$-enriched** *antamanide,* **cyclo-(-Val[1]-Pro[2]-Pro[3]-Ala[4]-Phe[5]-Phe[6]-Pro[7]-Pro[8]-Phe[9]-Phe[10]-), using quantitative numerical 2D NMR spectrum evaluation based on the product-operator formalism. The experimental basis comprises two-dimensional $^1H$, $^{13}C$-heteronuclear relayed E.COSY spectra [J. M. Schmidt, R. R. Ernst, S. Aimoto, and M. Kainosho,** *J. Biomol. NMR* **6, 95 (1995)], the multiplet patterns of which are subjected to iterative least-squares 2D multiplet-simulation procedures. Accuracy and precision of the spectrum fit are assessed by *F* statistics and analysis of variances (ANOVA) leading to confidence intervals for the optimized spin-system parameters. The long-range J coupling constants obtained and their standard deviations provide the experimental foundation for a later detailed analysis of $\phi$ and $\chi_1$ dihedral-angle equilibrium conformations contributing to the flexible peptide structure.** 

## INTRODUCTION

The determination of the three-dimensional solution structure of peptides and proteins by NMR spectroscopy (*1–6*) traditionally relies on proton–proton distance constraints as derived from proton–proton cross-relaxation (NOE) rates (*7*). Conformational analysis then is based on the often arbitrary assumption that the molecular structure is rigid, except for the component of overall reorientation in solution. Consequently, at the same time as the resolution of the molecular model increases during the geometry-refinement process, inconsistencies arise from the neglect of internal molecular mobility (*8–10*). As an additional complication, NOE effects in molecules like peptides, which have reorientational tumbling rates on the order of the $^1H$ Larmor frequency are extremely small and difficult to quantitate. Structure refinement is particularly limited in short polypeptide chains lacking pronounced secondary structure, so that long-distance NOE information is sparse if not absent. In such cases, rotating-frame NOE effects as exploited by ROESY (*11*) are an alternative to NOESY in obtaining distance constraints.

In recent years, conformational analysis has profited from the derivation of angular constraints obtained from the measurement of vicinal coupling constants (*12–14*), the magnitudes of which are connected with the dihedral-angle conformation through empirical Karplus relationships (*15, 16*). Because of the high abundance of the $^1H$ isotope, homonuclear $^3J_{HH}$ coupling constants have been determined traditionally. With the availability of stable-isotope enrichment procedures, heteronuclear $^3J_{HX}$ coupling constants, where X equals $^{15}N$ or $^{13}C$, can be measured with sensitivity to also provide dihedral-angle information (Fig. 1).

While numerous methods have been established to record the effect of *J* interaction, quantitative evaluation of the spectral patterns lags behind the improvement in experimental techniques. Similar to the situation of NOE, quantitative interpretation of $^3J$ coupling constants in terms of conformational restrictions also suffers from the assumptions mentioned above concerning molecular mobility. The present study therefore aims at developing the quantitative evaluation of dihedral-angle conformations and conformational equilibria on the exclusive basis of accurately determined values of $^3J$. The work is presented in two sections, this article which deals with a detailed procedure to extract accurate values of $^3J$ from 2D NMR multiplets, and the subsequent article which is devoted to the problem of predicting dihedral-angle conformations based on experimental $^3J$ coupling information. The methods are demonstrated on the naturally occuring cyclic decapeptide antamanide.

## ANTAMANIDE

The biologically active components of the poisonous mushroom *Amanita phalloides* compose two groups of cyclic peptides, the amatoxins and the phallotoxins, which have been found to cause fatal human mushroom intoxication (*17*). The action of these peptides ranges from RNA polymerase B inhibition to potassium-conductance block in hepatic membrane transport systems. From the same species, the unique cyclic peptide antamanide (–Val[1]–Pro[2]–Pro[3]–Ala[4]–Phe[5]–Phe[6]–Pro[7]–Pro[8]–Phe[9]–Phe[10]–) has been iso-



1090-7807/97 $25.00

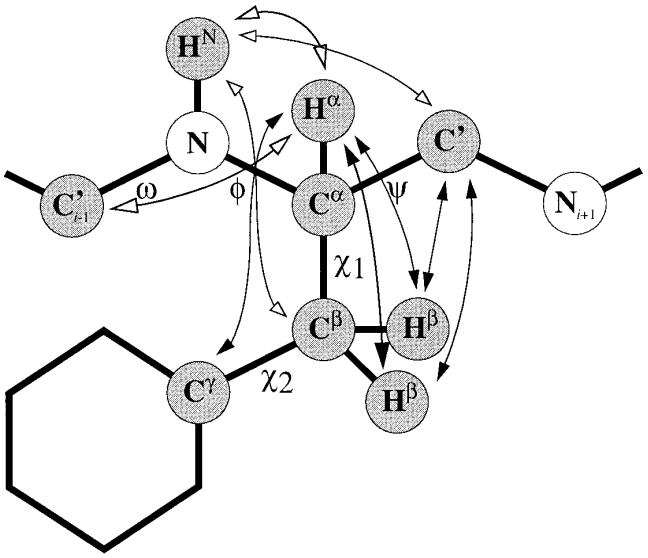


**FIG. 1.** Typical spin–spin coupling topology encountered in $^{13}$C-enriched polypeptides. The phenylalanine side chain is chosen as an example. Uniform $^{13}$C enrichment gives rise to a large number of line splittings. Shaded atoms are the NMR active spins accounted for in 2D multiplet simulations. Arrows indicate the homo- and heteronuclear three-bond couplings examined in the context of the present investigation. Conformationally relevant three-bond connectivities are indicated by white and black tips for $\phi$ and $\chi_1$ torsions, respectively.

lated, which protects from hepatocyte lesions because it antagonizes the phalloidin-induced negative inotropic effect (weakening of heart-muscle contractility) (*18–22*).

Although many derivatives of the native antamanide sequence have been designed, the specificity of the drug is not yet sufficiently understood. Antamanide has been investigated by a variety of analytical methods (*23–27*). These studies showed that the peptide exhibits molecular dynamics phenomena spanning different time scales (*28–38*). Slow backbone reorientational processes were found to occur in the microsecond range (*28–32*), while conformational heterogeneity of the phenylalanine side chains was associated with characteristic interconversion times in the nanosecond range (*33–35*). Finally, the proline residues undergo conformational interconversion on a picosecond time scale (*36–38*). All these dynamic processes lead to an averaging of both NOE cross-relaxation rates and three-bond coupling constants, thus rendering antamanide an excellent model to demonstrate methods for detecting conformational equilibria on the basis of spin–spin coupling constants.

Techniques for the extraction of homonuclear coupling constants from spectral patterns, such as DISCO (*39*), E.COSY (*40–42*), local-symmetry analysis (*43*), recursive multiplet contraction (*44*), and least-squares 2D multiplet fitting based on density-matrix calculations (*45*) have been developed using antamanide as a reference compound. Therefore, it is reasonable to refer to the known properties of antamanide when examining procedures to quantitate heteronuclear $^3J$ coupling constants. Recently, the heteronuclear relayed E.COSY pulse sequence (*46*), which is essentially a small-flip-angle variant of the 2D-heteronuclear multiple-quantum coherence (HMQC) correlation experiment (*47, 48*) with an additional COSY mixing pulse (*49*) was applied to a sample of uniformly $^{13}$C-labeled antamanide dissolved in chloroform. For a detailed description of the pulse sequence, the reader is referred to Ref. (*46*). Here, a numerical protocol for the simulation of E.COSY-type multiplet fine structure is proposed, the underlying aim of which is rapid computation in view of utility in automatic NMR processing and evaluation tools.

## METHODS

E.COSY initially relies on the coupling topology in a minimum three-spin fragment, where an active coupling between two spins is required to generate the 2D correlation multiplet, and two passive couplings to the third spin appear as modulations in the multiplet structure (*40–42*). Relayed E.COSY is based on a coupling topology extended to a minimum of four spins (*46, 50*). Examples for multiplet patterns typically observed in heteronuclear relayed E.COSY are displayed in Fig. 2. Characteristic tilts in the 2D multiplet patterns are observed in which the resonance-frequency difference between pairs of relevant E.COSY signal contributions (signified by $|\alpha\rangle$ and $|\beta\rangle$ states of the passive spin) yields the desired coupling constant. Usually, one seeks the translational relative shift along the $\omega_2$ dimension required to optimally superimpose the resolution-enhanced one-dimensional $\omega_2$ traces of the two multiplet halves, which are sufficiently separated along $\omega_1$ by a large coupling.

Manual alignment of resolution-enhanced 1D spectrum traces, taken through pairwise related components of the E.COSY multiplets (*42*), lacks an objective function to indicate the ''best'' superposition of the discretely sampled spectrum data. With stepwise trace alignment, the values for both the coupling constant and the associated error are necessarily integer multiples of the digital resolution in the $\omega_2$ dimension (*51*). The method of continuous trace alignment to superimpose 1D sections yields improved values and avoids the limitation of a discrete sampling grid (*46*). However, partial overlap of critical multiplet lines might spoil the determination of coupling constants by 1D methods, e.g., in the ($C^\alpha$, $H^N$) patterns of Ala$^4$, Phe$^5$, Phe$^9$, or Phe$^{10}$ depicted in Fig. 3. Furthermore, the two-dimensional E.COSY multiplet fine structure possesses centrosymmetric features (*52*) for which 1D trace projection (*39, 42*) and alignment methods (*46, 53*) generally do not account. Unless the constituent multiplet lines are well resolved, neglect of these details gives rise to incorrect, usually too small, $J$ values. Here, the recently recorded heteronuclear relayed E.COSY spectrum of antamanide (*46*) is re-evaluated, and it is demonstrated that full 2D multiplet simulation is capable of accounting for both overlap as well as $C_2$ symmetry specific to E.COSY multiplets (*52*). In view of the applicability to protein spectros-

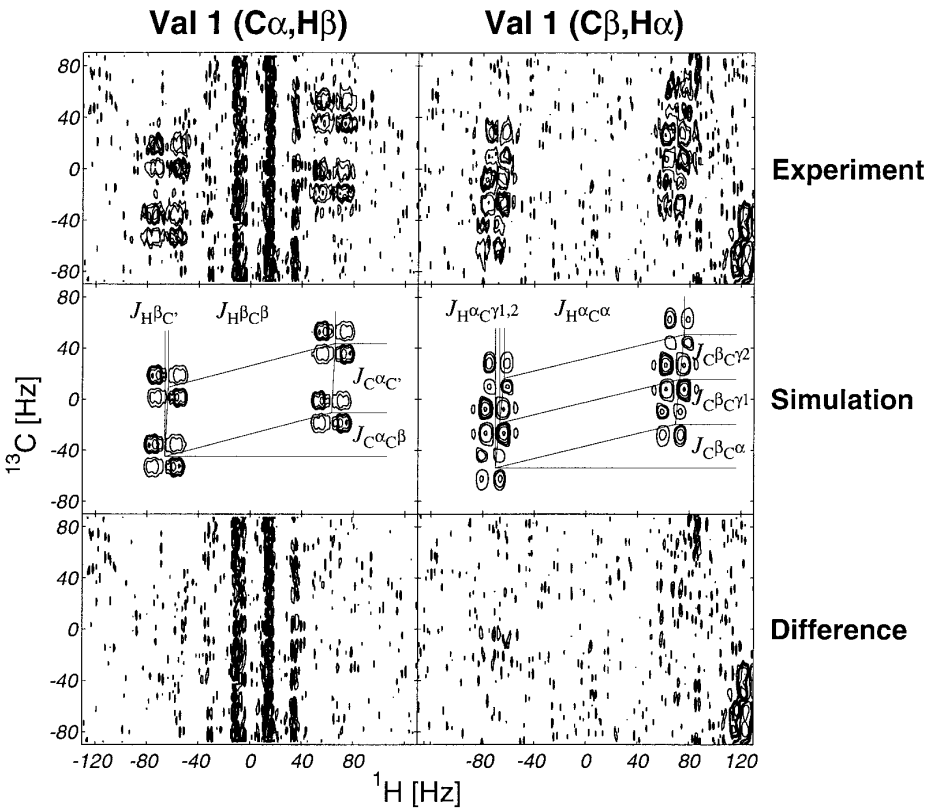


**FIG. 2.** Analysis of the side-chain correlations in the 2D heteronuclear relayed E.COSY spectrum of Val[1] in $^{13}$C-enriched antamanide in $CDCl_3$. The spectrum was recorded within 8 h at 500 MHz and 310 K using 20 m*M* sample concentration. For each $t_1$ increment, 16 transients were accumulated with the pulse sequence and phase combinations given in Ref. (*46*). The acquisition times were 68 and 369 ms in $t_1$ and $t_2$ dimensions, corresponding to 1K and 4K recorded data points, respectively. Total carbon and proton spectral widths were 7576 and 5556 Hz in $\omega_1$ and $\omega_2$ dimensions, respectively. TPPI was used for phase sensitive detection in the $\omega_1$ dimension. Spectrum processing included sine-bell filtering and Fourier transformation to 1K × 4K real points using zero filling once in each dimension to yield spectral resolutions of 7.398 and 1.356 Hz in $\omega_1$ and $\omega_2$, respectively. Both components, pure absorptive (displayed) and pure dispersive (not shown), were retained to facilitate the convergence in least-squares multiplet fits. Contours are drawn for positive and negative levels with spacings of $\sqrt{2}$ and 2, respectively, starting at twice the RMS noise amplitude. The left panels show the ($C^{\alpha}$, $H^{\beta}$) = (56.3 ppm, 2.04 ppm) multiplet reconstruction with two pairs of passive E.COSY couplings indicated, from which the $^3J(H^{\beta}, C')$ coupling constant was taken. The right panels show the ($C^{\beta}$, $H^{\alpha}$) = (30.7 ppm, 4.46 ppm) multiplet reconstruction yielding the pair of $^3J(H^{\alpha}, C^{\gamma})$ coupling constants which is hardly accessible by 1D trace examination. The difference patterns exhibit artifacts arising from $t_1$ noise.

copy, where spectra suffer from even larger linewidths than those of peptides, iterative computer fitting is proposed for extracting accurate coupling constants and their associated errors.

*Strategies for Computer Implementation*

Highly automated spectral analysis demands efficient fit algorithms, since iterative optimization of multiple-parameter problems requires continuously repeated computations. In particular when applied to spectra of isotope-labeled biomolecules, where spin systems typically comprise many coupled nuclei, Hamiltonian-based approaches would involve a prohibitively large number of matrix products, even if relaxation effects are neglected. The complexity is expected to increase with $N^3$ where $N$ is the dimension of the Hilbert space (*54*), and therefore density-matrix algorithms (*54, 55*), although they allow exact modeling of spectral responses, are not feasible for routine use with respect to today's computer resources.

The rationale of the algorithm proposed here is that the effects of lineshape parameters associated with $\omega_1$ and $\omega_2$ are completely separable in the limit of weak coupling. This allows for construction of the 2D multiplet matrix from simple products of $\omega_1$ and $\omega_2$ projection vectors. Based on the product-operator formalism (*56*), the computation of the 1D projections themselves then necessitates convolving chemical-shift and lineshape contributions as well as an appropriate set of signed $J$ splittings. In practice, advantage is taken of Fourier transform (FT) theorems so that spectrum representation basically involves the construction of the respective 1D time-domain free-induction decays according to

$$F(\omega_1, \omega_2) = F(\omega_1) \times F(\omega_2) = \mathbf{FT}\{f(t_1)\} \times \mathbf{FT}\{f(t_2)\}. \quad [1]$$

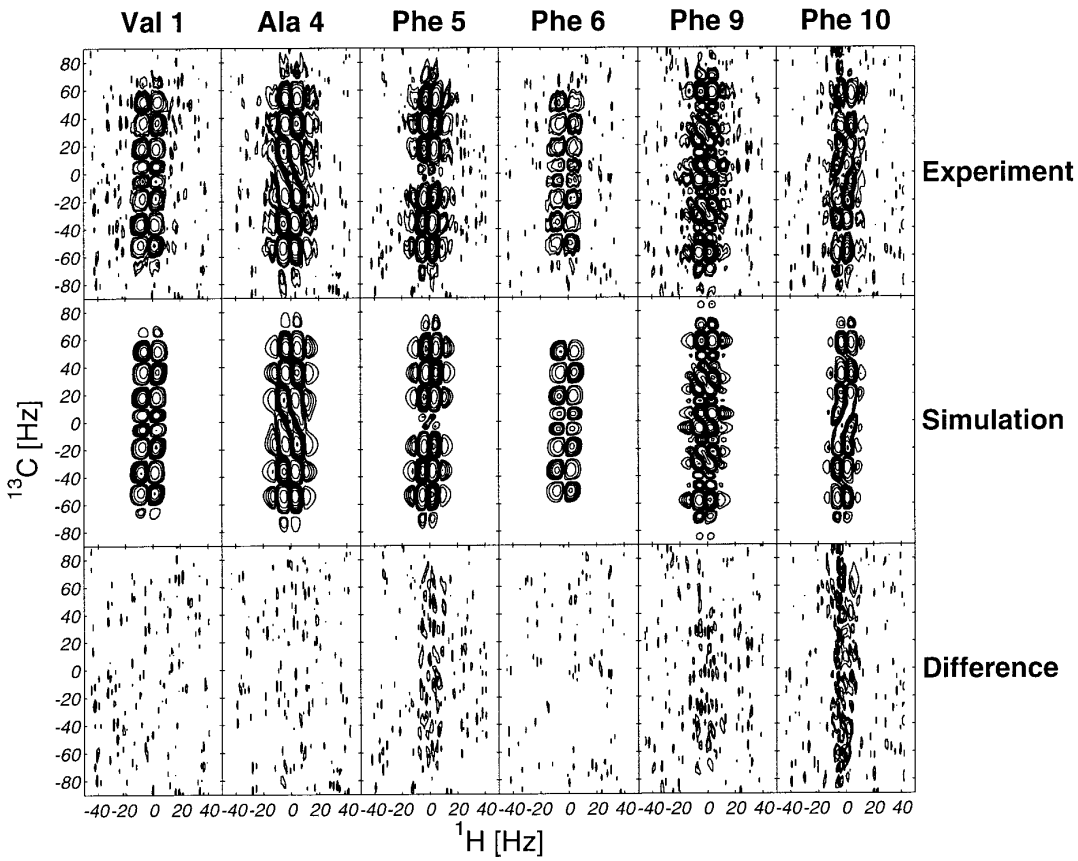


**FIG. 3.** Pure 2D absorption mode representation of the ($C^{\alpha}$, $H^{N}$) correlation multiplets of the nonproline residues in the 2D heteronuclear relayed E.COSY spectrum of $^{13}$C-enriched antamanide. From these cross peaks, the heteronuclear coupling constants $^{3}J(H^{N}, C^{\beta})$ and $^{3}J(H^{N}, C')$ were determined. At 310 K, the multiplets are located at ($\omega_1$, $\omega_2$) coordinates, given in ppm: Val[1] (56.4, 7.57), Ala[4] (49.6, 7.95), Phe[5] (56.7, 6.96), Phe[6] (52.2, 7.81), Phe[9] (57.3, 7.35), and Phe[10] (58.9, 7.24). For further experimental details, see the legend to Fig. 2.

The constituent product operators $f(t)$ are summarized in Table 1.

The complexity of the proposed algorithm is dominated by the number $n$ of passively coupled E.COSY-type spins $\frac{1}{2}$ and increases with order $O(2^n rc)$, where $r$ and $c$ denote row and column projection-vector sizes, respectively. Due to the very distinct approaches of product-operator and density-matrix-based algorithms, comparison of the computational costs can only be approximate. Considering identical multiplet-spectrum sizes, the proposed scheme is expected to save at least a factor of $2^{2n}$ at the expense of exact treatment of strong-coupling effects. Calculation of projections is significantly accelerated through the use of highly vectorized fast Fourier transforms (FFT) when computing larger multiplet matrices. All these advantages can be utilized to treat sizeable spin-coupling topologies like those encountered in isotopically enriched amino acids.

**TABLE 1**
**Constituent Product Operators Used for Time-Domain FFT Construction of 1D Multiplet Projections**

| Parameter type | Function | Gradient |
|---|---|---|
| Amplitude-scaling factor | $f(t) = A$ | $\partial f(t)/\partial A = f(t)/A$ |
| Apparent linewidth | $f(t) = \exp(-\pi R t)$ | $\partial f(t)/\partial R = (-\pi t)\exp(-\pi R t)$ |
| Position[a] | $f(t) = \exp(i2\pi v t)$ | $\partial f(t)/\partial v = (i2\pi t)\exp(i2\pi v t)$ |
| Anti-phase splitting | $f(t) = i\sin(\pi J t)$ | $\partial f(t)/\partial J = (i\pi t)\cos(\pi J t)$ |
| In-phase splitting | $f(t) = \cos(\pi J t)$ | $\partial f(t)/\partial J = (-\pi t)\sin(\pi J t)$ |

[a] The positional parameter $v$ refers to the center coordinates of the selected multiplet submatrix.

*Gradient Evaluations*

In view of efficient multiple-parameter optimization, it is desirable to drive the function optimizer by providing analytical derivatives with respect to each model parameter. The use of product operators for describing NMR multiplets typically involves trigonometric and exponential terms, the analytical derivatives of which are particularly simple to formulate and do not require excess floating-point operations compared to evaluation of the function itself (Table 1). Recourse to robust yet inefficient finite-difference techniques, like the SIMPLEX procedure (*57*), is thus avoided. The ma-

jor task is calculating gradients for those parameters that cannot be uniquely assigned to a specific spectrum dimension, for example, the gradient with respect to the active anti-phase splitting in a COSY-type multiplet $f(t_1, t_2) = \sin(\pi J t_1)\sin(\pi J t_2)$. The partial derivative associated with the $J$ value then results from a superposition of two gradient matrices constructed according to

$$\begin{aligned}\frac{\partial f(t_1, t_2)}{\partial J} &= \frac{\partial f(t_1)}{\partial J} + \frac{\partial f(t_2)}{\partial J} \\ &= \pi t_1 \cos(\pi J t_1)\sin(\pi J t_2) \\ &\quad + \pi t_2 \sin(\pi J t_1)\cos(\pi J t_2). \end{aligned} \quad [2]$$

*E.COSY-type Multiplets*

Compared to COSY, the symmetry encountered in E.COSY-type multiplets is reduced (*52*) under the influence of a passive spin $p$ with resolved couplings to the spin pair $kl$. The effect is numerically accomplished by the weighted superposition of in-phase and anti-phase splitting patterns according to

$$\begin{aligned} f(t_1, t_2) &= \cos(\pi J_{kp} t_1)\cos(\pi J_{lp} t_2) \\ &\quad - \cos(\beta)\sin(\pi J_{kp} t_1)\sin(\pi J_{lp} t_2), \end{aligned} \quad [3]$$

where $\beta$ is the flip angle of the final carbon mixing pulse in the standard heteronuclear relayed E.COSY experiment (*46*), and is substituted for $(\pi\text{-}\beta)$ in the complementary E.COSY experiment. If phase cycling procedures are applied, $\beta = 0$, which leads to perfect suppression of undesired multiplet components. The fact that the operations of multiplicative matrix expansion (Eq. [1]) and subtractive superposition (Eq. [3]) do not commute requires two separate calculations, which are finally combined to obtain the simulated E.COSY pattern. The effect of multiple passive spins due to uniform $^{13}$C isotope enrichment is modeled by cascading the procedure outlined in Eq. [3].

*Strong-Coupling Approximation*

A simple extension to the basic algorithm makes it possible to incorporate first-order strong-coupling effects (*58*) and is found to significantly improve the results. The strong-coupling parameter $C$ is defined to agree with the usual conventions (*59*)

$$C_{kl} = \tfrac{1}{2}(\omega_0^2 \delta_{kl}^2 + J_{kl}^2)^{1/2}, \quad [4]$$

where the index specifies the pair of coupled nuclei $k$ and $l$. It is convenient to express the strong-coupling parameter $C_{kl}$ as a dimensionless quantity $\theta$ which no longer depends on the magnetic field $\omega_0$ actually applied or on the chemical-shift difference $\delta_{kl}$ and which has the properties

$$\begin{aligned} 2\theta_{kl} &= \operatorname{atan}[J_{kl}/(\omega_0 \delta_{kl})]; \\ \sin 2\theta_{kl} &= J_{kl}/2C_{kl}; \\ \cos 2\theta_{kl} &= \omega_0 \delta_{kl}/2C_{kl}; \end{aligned} \quad [5]$$

where $\theta_{kl} = 0$ in the limit of weak coupling. The intensity ratio of ''inner'' and ''outer'' lines in the spectrum of a coupled two-spin-$\frac{1}{2}$ system is then given by $(1 + \sin 2\theta)/(1 - \sin 2\theta)$, from which it follows that the time-domain equivalent for approximating strong-coupling effects is a superposition of two counterrotating complex exponentials with the respective intensities. The trigonometric product operators are thus extended (*60*) by a properly scaled imaginary component as exemplified for a COSY-type in-phase multiplet splitting.

$$\begin{aligned} f(t) &= \tfrac{1}{2}\{(1 + \sin 2\theta_{kl})\exp(i\pi J_{kl} t) \\ &\quad + (1 - \sin 2\theta_{kl})\exp(-i\pi J_{kl} t)\} \\ &= \cos(\pi J_{kl} t) + i \sin 2\theta_{kl} \sin(\pi J_{kl} t). \end{aligned} \quad [6]$$

## COMPUTATIONS

*Multiplet Model Function*

In order to extract accurate $^3J(\mathrm{H^N}, \mathrm{C}')$ and $^3J(\mathrm{H^N}, \mathrm{C}^\beta)$ coupling constants, the tilted 2D E.COSY-type $(\mathrm{C}^\alpha, \mathrm{H^N})$ multiplet patterns in Fig. 3 were reconstructed by least-squares spectrum simulation. Iterative time-domain Fourier synthesis of $\omega_1$ and $\omega_2$ spectrum projections with subsequent matrix expansion yielded the 2D frequency-domain splitting patterns $M^{\mathrm{calc}}(\omega_1, \omega_2)$. Considering a cyclic four-spin coupling topology $(-I_2-I_1-S_1-S_2-)$ with nonvanishing *relayed* $(S_1 \rightarrow I_1 \rightarrow I_2)$ and *direct* $(S_1 \rightarrow I_2)$ transfer couplings, the coupling constant $^3J(\mathrm{H^N}, \mathrm{C}')$ is accessible if $I_2$, $I_1$, $S_1$, and $S_2$ are identified with $\mathrm{H^N}$, $\mathrm{H}^\alpha$, $\mathrm{C}^\alpha$, and $\mathrm{C}'$, respectively (*61*). In the weak-coupling limit, the time-domain modulations of the detected $(S_1, I_2)$ signal are given by

$$\begin{aligned} f(t_1, t_2) &= \exp(i\Omega_{\mathrm{C}^\alpha} t_1)\exp(i\Omega_{\mathrm{H^N}} t_2) \\ &\quad \times \cos(\pi J_{\mathrm{H^N C}^\alpha} t_2)\sin(\pi J_{\mathrm{H^N H}^\alpha} t_2)\sin(\beta) \\ &\quad \times \{\sin(\pi J_{\mathrm{H^N C}^\alpha} t_1)\cos[\pi J_{\mathrm{H^N H}^\alpha}(t_1 + 2\tau)] \\ &\quad\quad - \cos(\pi J_{\mathrm{H^N C}^\alpha} t_1)\sin[\pi J_{\mathrm{H^N H}^\alpha}(t_1 + 2\tau)]\} \\ &\quad \times \prod_k \{\cos(\pi J_{\mathrm{C}^\alpha \mathrm{C}^k} t_1)\cos(\pi J_{\mathrm{H^N C}^k} t_2) \\ &\quad\quad - \cos(\beta)\sin(\pi J_{\mathrm{C}^\alpha \mathrm{C}^k} t_1)\sin(\pi J_{\mathrm{H^N C}^k} t_2)\} \\ &\quad \times \prod_l \cos[\pi J_{\mathrm{H}^\alpha \mathrm{H}^l}(t_1 + 2\tau)]\cos(\pi J_{\mathrm{H^N H}^l} t_2), \end{aligned} \quad [7]$$

where $\beta = 35°$ and $\tau = (2J_{\mathrm{C}^\alpha \mathrm{H}^\alpha})^{-1} = 3.57$ ms represent the flip angle of the carbon mixing pulse and the fixed delay time for evolution of one-bond H, C couplings, respectively

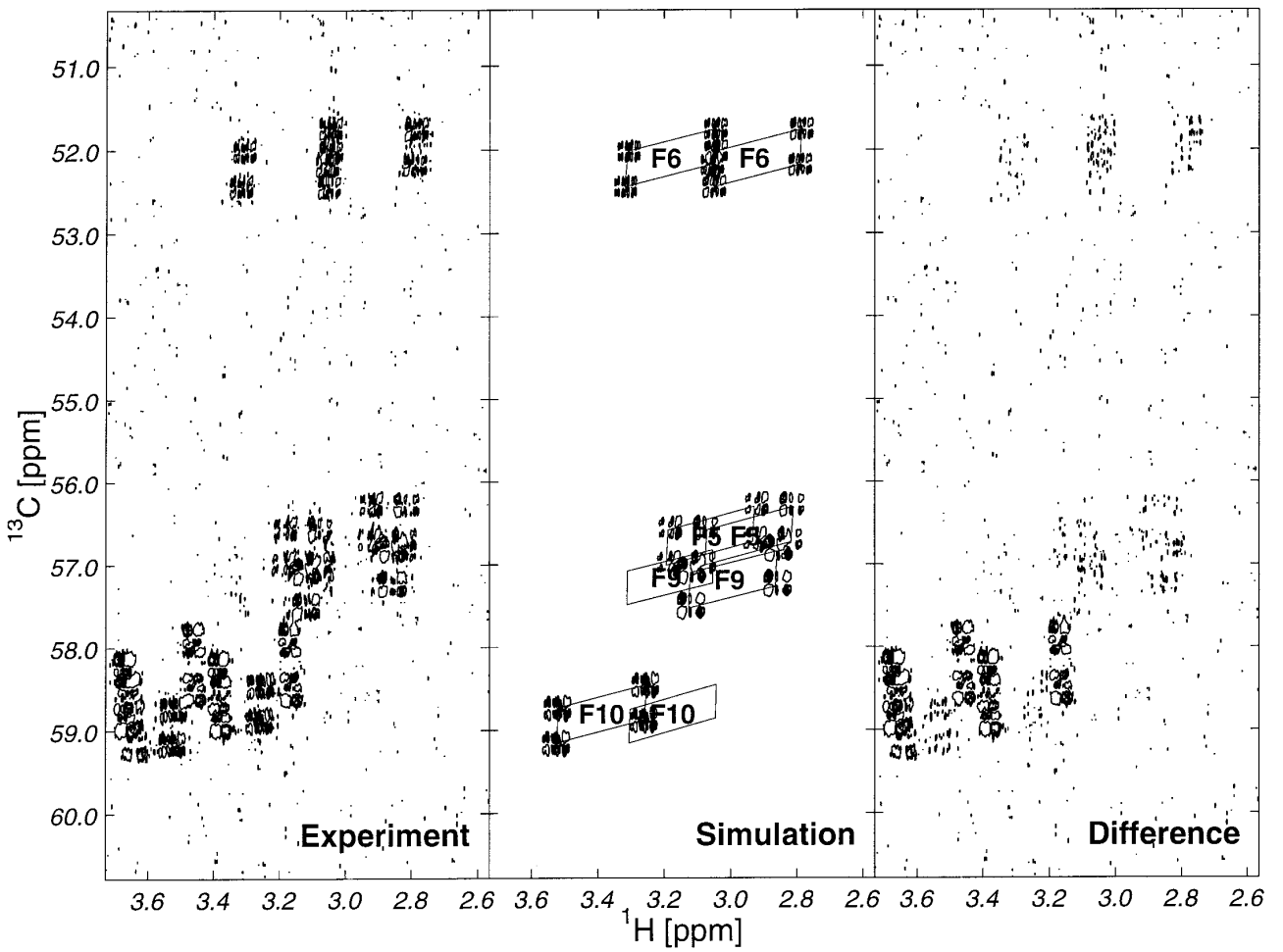


**FIG. 4.** Excerpt from the 2D heteronuclear relayed E.COSY spectrum of $^{13}$C-enriched antamanide showing ($C^{\alpha}$, $H^{\beta}$) correlation multiplets of the phenylalanine residues. Positive and negative intensities are indicated by dense and sparse contour levels, respectively, with the lowest level at three times the RMS noise amplitude. The parallelograms connect the four constituent multiplet parts where the edges represent splittings due to the passive couplings $^{1}J(C^{\alpha}, C')$ and $^{1}J(C^{\alpha}, C^{\beta})$ along $\omega_1$ and $^{1}J(H^{\beta}, C^{\beta})$ and $^{3}J(H^{\beta}, C')$ along $\omega_2$. Quantitative evaluation of the desired heteronuclear coupling constant $^{3}J(H^{\beta}, C')$ was achieved by full multiplet simulation, taking strong-coupling effects into account as described in the text. The difference intensity is due to the ($C^{\alpha}$, $H^{\alpha}$) auto-correlation signals of Pro[2] and Pro[7]. The ($C^{\alpha}$, $H^{\beta 3}$) correlations of Phe[9] and Phe[10] could be analyzed despite their small intensity. For further experimental details, see the legend to Fig. 2.

(*46*). While the first part of Eq. [7] includes shared multiplet position, splitting modulation, and flip-angle dependence, the subsequent term comprises splitting modulations specific to either the direct (sine-cosine dependence) or the relayed (cosine-sine dependence) path. Product operators indexed by $k$ and $l$ run over those passive carbon ($C'$, $C^{\beta}$, $C^{\gamma}$, $C^{\delta}$, $C'_{i-1}$) and proton ($H^{\beta}$, $H^{\gamma}$, $H^{\delta}$) spins that cause E.COSY (Eq. [3]) and COSY-type multiplet splittings, respectively. Similarly, $^{3}J(H^{\beta}, C')$ coupling constants can be determined from ($C^{\alpha}$, $H^{\beta}$) multiplets based on the four-spin coupling topology comprising $H^{\beta}$, $H^{\alpha}$, $C^{\alpha}$, and $C'$ (Fig. 4), while the determination of $^{3}J(H^{\alpha}, C^{\gamma})$ coupling constants from ($C^{\beta}$, $H^{\alpha}$) multiplets involves $H^{\alpha}$, $H^{\beta}$, $C^{\beta}$, and $C^{\gamma}$ (Fig. 5). The types and numbers of passive spins depend on the amino-acid type and vary for the different correlation patterns as summarized in Table 2 for the phenylalanine spin topology. The ($t_1$, $t_2$) free-induction decay signals computed from Eq. [7] were supplemented by apodization functions identical to those used in spectrum processing, i.e., $h(t_1, t_2) = \sin(\pi t_1/t_1^{\max})\sin(\pi t_2/t_2^{\max})$.

### *Optimization Protocol*

Including an amplitude scaling factor, a total of 15 adjustable and 4 fixed parameters was needed to construct the synthetic multiplets (Table 2). In simulations of the phenylalanine multiplets, the proton–proton couplings giving rise to COSY-type in-phase splittings were excluded from iteration, because $H^{\beta x}$ and $H^{\beta y}$ sites are numerically indistinguishable. The homonuclear coupling constants involved were therefore fixed to the known values given in Ref. (*42*). However, the unique proton–proton anti-phase splitting due to the ac-

**TABLE 2**
**Control Parameters Used in Modeling of 2D Heteronuclear Relayed E.COSY Multiplets**

| Parameter type | Dimension | Parameter association: ($C^{\alpha}$, $H^{N}$) multiplet | ($C^{\alpha}$, $H^{\beta}$) multiplet[a] | ($C^{\beta}$, $H^{\alpha}$) multiplet[b] |
|---|---|---|---|---|
| | | Function evaluation | | |
| Amplitude-scaling factor | — | $A$ | $A$ | $A$ |
| Apparent linewidth | $\omega_1$ | $R(C^{\alpha})$ | $R(C^{\alpha})$ | $R(C^{\beta})$ |
| Apparent linewidth | $\omega_2$ | $R(H^{N})$ | $R(H^{\beta x})$ | $R(H^{\alpha})$ |
| Position[c] | $\omega_1$ | $v(C^{\alpha})$ | $v(C^{\alpha})$ | $v(C^{\beta})$ |
| Position | $\omega_2$ | $v(H^{N})$ | $v(H^{\beta x})$ | $v(H^{\alpha})$ |
| Direct-transfer coupling | $\omega_1$, $\omega_2$ | $^2J(C^{\alpha}, H^{N})$ | $^2J(C^{\alpha}, H^{\beta x})$ | $^2J(C^{\beta}, H^{\alpha})$ |
| Relayed-transfer coupling | $\omega_1$, $\omega_2$ | $^3J(H^{N}, H^{\alpha})$ | $^3J(H^{\beta x}, H^{\alpha})$ | $^3J(H^{\alpha}, H^{\beta x})$ or $^3J(H^{\alpha}, H^{\beta y})$ |
| E.COSY in phase splitting | $\omega_1$ | $^1J(C^{\alpha}, C_i')$ | $^1J(C^{\alpha}, C^{\beta})$ | $^1J(C^{\beta}, C^{\alpha})$ |
| E.COSY in phase splitting | $\omega_2$ | $^3J(H^{N}, C_i')$ | $^1J(H^{\beta x}, C^{\beta})$ | $^1J(H^{\alpha}, C^{\alpha})$ |
| E.COSY in phase splitting | $\omega_1$ | $^1J(C^{\alpha}, C^{\beta})$ | $^1J(C^{\alpha}, C_i')$ | $^1J(C^{\beta}, C^{\gamma})$ |
| E.COSY in phase splitting | $\omega_2$ | $^3J(H^{N}, C\beta)$ | $^3J(H^{\beta x}, C_i')$ | $^3J(H^{\alpha}, C^{\gamma})$ |
| E.COSY in phase splitting | $\omega_1$ | $^2J(C^{\alpha}, C_{i-1}')$ | $^2J(C^{\alpha}, C^{\gamma})$ | $^2J(C^{\beta}, C^{\delta})$[d] |
| E.COSY in phase splitting | $\omega_2$ | $^2J(H^{N}, C_{i-1}')$ | $^2J(H^{\beta x}, C^{\gamma})$ | $^4J(H^{\alpha}, C^{\delta})$ |
| E.COSY in phase splitting | $\omega_1$ | $^1J(C^{\alpha}, C^{\gamma})$ | $^3J(C^{\alpha}, C^{\delta})$ | $^2J(C^{\beta}, C_i')$ |
| E.COSY in phase splitting | $\omega_2$ | $^4J(H^{N}, C^{\gamma})$ | $^3J(H^{\beta x}, C^{\delta})$ | $^2J(H^{\alpha}, C_i')$ |
| COSY in phase splitting[e] | $\omega_1$ | $^3J(H^{\alpha}, H^{\beta x})$ | $^3J(H^{\alpha}, H^{N})$ | $^3J(H^{\beta x}, H^{\beta y})$ |
| COSY in phase splitting | $\omega_2$ | $^4J(H^{N}, H^{\beta x})$ | $^4J(H^{\beta x}, H^{N})$ | $^3J(H^{\alpha}, H^{\beta y})$ or $^3J(H^{\alpha}, H^{\beta x})$ |
| COSY in phase splitting | $\omega_1$ | $^3J(H^{\alpha}, H^{\beta y})$ | $^3J(H^{\alpha}, H^{\beta y})$ | $^4J(H^{\beta x}, H^{N})$ or $^4J(H^{\beta y}, H^{N})$ |
| COSY in phase splitting | $\omega_2$ | $^4J(H^{N}, H^{\beta y})$ | $^2J(H^{\beta x}, H^{\beta y})$ | $^3J(H^{\alpha}, H^{N})$ |
| | | Error calculation | | |
| Numerator degrees of freedom ($p - 1$) | | 14 | 14 | 16 |
| Denominator degrees of freedom ($n - p$) | | 2033 | 4593 | 4591 |
| *F ratio* | | 1.372 | 1.370 | 1.347 |
| $\epsilon^2$ ratio | | 1.0094 | 1.0042 | 1.0047 |

[a] Irrespective of stereospecific resonance assignments, *low-field* and *high-field* resonances in the phenylalanine coupling topology according to Fig. 1 are signified by *x* and *y*, respectively.

[b] The presence of two methylene $H^{\beta}$ relay protons necessitates superimposing two relayed E.COSY patterns in a simultaneous fit to represent the ($C^{\beta}$, $H^{\alpha}$) multiplet. Active homonuclear transfer couplings were weakly constrained to the values given in Ref. (*42*) by applying a penalty as described in the text.

[c] Positional parameters refer to the center coordinates of the selected multiplet submatrix.

[d] In $Val^1$, $C^{\gamma x}$ and $C^{\gamma y}$ are substituted for $C^{\gamma}$ and $C^{\delta}$, respectively.

[e] In-phase splittings due to homonuclear couplings were fixed to the values given in Ref. (*42*).

tive COSY-type transfer coupling was treated as a freely adjustable parameter in simulations of the ($C^{\alpha}$, $H^{N}$) and ($C^{\alpha}$, $H^{\beta}$) multiplets, except for the compound ($C^{\beta}$, $H^{\alpha}$) multiplets in which mild constraints prevented the pair of active $^3J_{HH}$ coupling constants from collapsing to an intermediate value. A parabolic penalty term, $\epsilon^2_{cons} = k_{cons}(J - J_0)^2$, with $J_0$ the target value, was added to the sum of squared residuals $\epsilon^2$ that drives the line search. The weighting factor $k_{cons}$ was conservatively chosen to represent the number of deviates considered in the residual in order to consume one degree of freedom for a 1 Hz constraint violation.

Initial values for the multiplet displacements $\nu_1$ and $\nu_2$ as well as for the E.COSY coupling parameters such as $^1J(H^{\beta}, C^{\beta})$, $^1J(C^{\alpha}, C^{\beta})$, $^1J(C^{\alpha}, C')$, and $^3J(H^{\beta}, C')$ in a ($C^{\alpha}$, $H^{\beta}$) correlation multiplet, were derived from pairwise coordinate differences between the four major multiplet constituents. Other $J_{CC}$ and $J_{HC}$ couplings were initialized at 1 Hz, while $J_{HH}$ couplings were initialized as previously determined (*42*). Parameters for the apparent half-height linewidth $R$ were initially set to 5 Hz.

The refinement protocol included an iterative least-squares optimization based on the BFGS quasi-Newton method (*62–65*). Overlapping multiplets were iterated in an interleaved manner to account for covariance effects, e.g., the ($C^{\alpha}$, $H^{\beta}$) and ($C^{\beta}$, $H^{\alpha}$) multiplets in Fig. 4 and Fig. 5, respectively. Analytical partial derivatives $\partial M_i/\partial P_j$ of the multiplet points $M_i$ with respect to each of the fit parameters $P_j$ were provided to drive the mixed quadratic and cubic line search algorithm. Typically, each multiplet simulation converged after 1000 function and 300 gradient evaluations, requiring approximately 4 CPU h on an Intel 486/50-based personal computer.

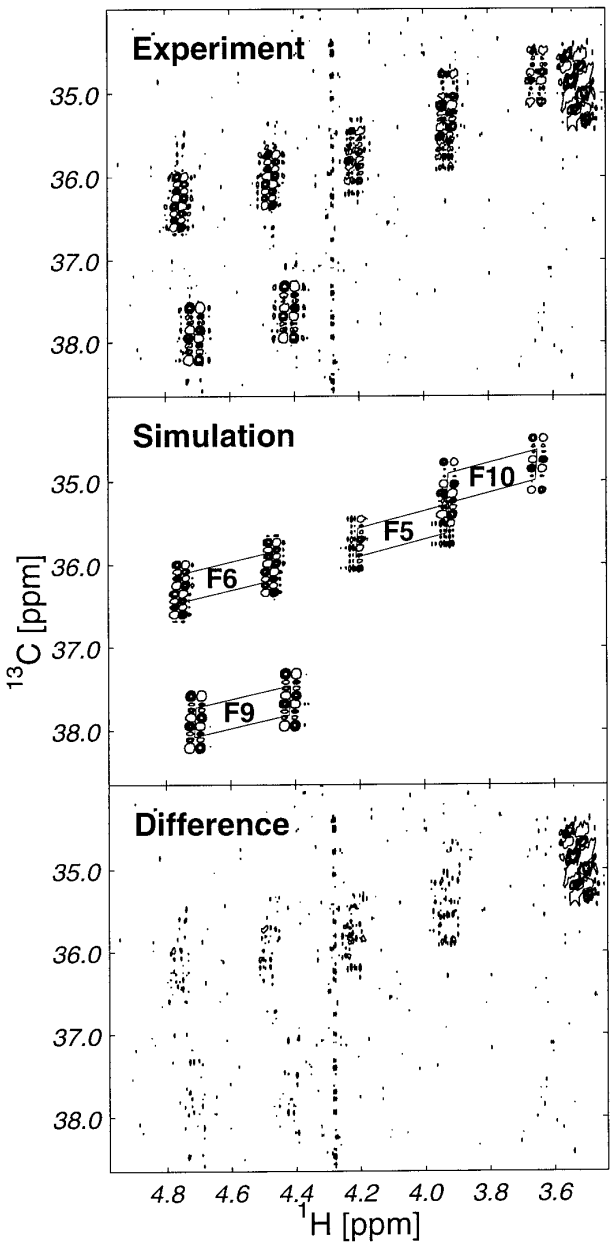


**FIG. 5.** Excerpt from the 2D heteronuclear relayed E.COSY spectrum of $^{13}$C-enriched antamanide showing ($C^{\beta}$, $H^{\alpha}$) correlation multiplets of the phenylalanine residues. Positive and negative intensities are indicated by dense and sparse contour levels, respectively, with the lowest level at three times the RMS noise amplitude. The parallelograms connect the four constituent multiplet parts where the edges represent splittings due to the passive couplings $^{1}J(C^{\beta}, C^{\gamma})$ and $^{1}J(C^{\beta}, C^{\alpha})$ along $\omega_1$ and $^{1}J(H^{\alpha}, C^{\alpha})$ and $^{3}J(H^{\alpha}, C^{\gamma})$ along $\omega_2$. Quantitative evaluation of the desired heteronuclear coupling constant $^{3}J(H^{\alpha}, C^{\gamma})$ was achieved by full multiplet simulation as described in the text. The difference intensity is due to a partial Phe[10] ($C^{\beta}$, $H^{\beta x}$) autocorrelation signal and artifacts arising from $t_1$ noise. For further experimental details, see the legend to Fig. 2.

### *Error Calculation*

The agreement between calculated and experimental data was characterized by the normalized fit error, $\epsilon^2 = \epsilon_{\text{noise}}^{-2} \Sigma_i^n (M_i^{\text{expt}} - M_i^{\text{calc}})^2$, where $i$ runs over $n$ tagged multiplet points and $\epsilon_{\text{noise}}^2$ is the mean squared-noise amplitude. The precision of the coupling constants determined was assessed by analysis of variances (ANOVA) to avoid significant underestimation of errors due to the intrinsic nonlinear properties of the model function. Three assumptions were made: (*i*) the parameter manifold obeys a multivariate Gaussian normal distribution, (*ii*) the spectrum points are not correlated, and (*iii*) the points are subject exclusively to uniform random errors (*66*). Hence, confidence boundaries for the parameters were derived from the fractional increase in the sum of squares of residuals computed according to

$$\frac{\epsilon_{\text{max}}^2}{\epsilon_{\text{min}}^2} = 1 + \frac{p-1}{n-p} F(p-1, n-p, \alpha), \qquad [8]$$

where $F$ is the Fisher variance ratio. Given the numbers of degrees of freedom, $p = 15$ and $n = 24 \times 192$, except for ($C^{\alpha}$, $H^{N}$) multiplet simulations in which $n = 32 \times 64$, critical $F$ values were calculated for a two-tailed test of the $F$-distribution function (*67*, *68*) using a rejection level of $\alpha = (1 - 0.683)/2$ associated with one Gaussian standard deviation. Table 2 gives a survey of the control parameters used for error calculation in the different situations. A modified secant algorithm (*69*) was used to change the optimized $^{3}J_{\text{HC}}$ coupling values until the sum of squares of the residuals reached the threshold $\epsilon_{\text{max}}^2$. A bidirectional search using positive and negative deflections in each parameter (*70*) showed negligible asymmetry of the $\epsilon^2$ isocontour on the multidimensional error hypersurface. The conformationally relevant $J$ coupling constants and the respective uncertainties are summarized in Table 3.

## RESULTS

### *$^{3}J_{HC}$ Coupling Constants in Antamanide*

From a single heteronuclear relayed E.COSY experiment on uniformly $^{13}$C-enriched antamanide, numerous heteronuclear three-bond coupling constants, including $^{3}J(H^{N}, C')$, $^{3}J(H^{N}, C^{\beta})$, $^{3}J(H^{\beta}, C')$, and $^{3}J(H^{\alpha}, C^{\gamma})$, were determined in a quantitative fashion using exhaustive 2D multiplet simulation. The coupling constants obtained are useful for stereospecific proton resonance assignments as well as for the determination of the $\phi$ and $\chi_1$ dihedral-angle values in the amino-acid backbone and side chains, respectively. The $^{3}J_{\text{HC}}$ coupling constants determined in this work supplement the homonuclear $^{3}J_{\text{HH}}$ coupling constants $^{3}J(H^{N}, H^{\alpha})$ and $^{3}J(H^{\alpha}, H^{\beta})$ reported previously (*26*, *28*, *42*). The extended sets of coupling constants and their associated experimental uncertainties, $J^{\text{expt}}$ and $\sigma_{J^{\text{expt}}}$, respectively, are summarized in Table 3 for valine, alanine, and phenylalanine residues in antamanide.

The coupling constants $^{3}J(H^{N}, C')$ and $^{3}J(H^{N}, C^{\beta})$ were evaluated from the ($C^{\alpha}$, $H^{N}$) correlation multiplets as de-

**TABLE 3**
**Summary of Experimental $^3J$ Coupling Constants (Hz) for the Nonproline Residues in Antamanide as Obtained from 2D Heteronuclear Relayed E.COSY Multiplet Simulation[a]**

| | Phe[5] | Phe[6] | Phe[9] | Phe[10] | Val[1] | Ala[4] |
|---|---|---|---|---|---|---|
| $^3J(H^N, H^\alpha)$ | 7.19 ± 0.06 | 6.72 ± 0.20 | 8.29 ± 0.11 | 7.60 ± 0.20 | 7.48 ± 0.10 | 8.60 ± 0.07 |
| $^3J(H^N, C'_i)$ | 1.47 ± 0.06 | 1.84 ± 0.21 | −0.02 ± 0.12 | 2.74 ± 0.15 | 1.23 ± 0.16 | 0.05 ± 0.06 |
| $^3J(H^N, C^\beta)$ | 1.56 ± 0.06 | 1.22 ± 0.23 | 2.10 ± 0.08 | 0.84 ± 0.13 | 1.32 ± 0.17 | 1.86 ± 0.06 |
| $^3J(H^\alpha, C'_{i-1})$[b] | 5.60 ± 1.00 | 2.00 ± 1.00 | 2.00 ± 1.00 | 6.80 ± 1.00 | 2.00 ± 1.00 | 2.00 ± 1.00 |
| $^3J(H^\alpha, H^{\beta x})$[c] | 6.63 ± 0.06 | 5.68 ± 0.01 | 4.08 ± 0.01 | 11.10 ± 0.03 | | |
| $^3J(H^\alpha, H^{\beta y})$[c] | 7.96 ± 0.02 | 5.83 ± 0.01 | 12.56 ± 0.02 | 4.01 ± 0.05 | | |
| $^3J(H^\alpha, C^\gamma)$ | 3.18 ± 0.14 | 4.85 ± 0.15 | 2.18 ± 0.20 | 2.89 ± 0.21 | | |
| $^3J(H^{\beta x}, C')$ | 2.78 ± 0.15 | 5.33 ± 0.09 | 0.24 ± 0.98 | 2.34 ± 0.11 | | |
| $^3J(H^{\beta y}, C')$ | 3.93 ± 0.17 | 2.60 ± 0.10 | 2.52 ± 0.19 | 1.43 ± 1.70 | | |

[a] $^3J_{HH}$ and $^3J_{HC}$ coupling constants of the valine and alanine side chains are discussed in the text.

[b] $^3J(H^\alpha, C'_{i-1})$ coupling constants and standard deviations were taken from Ref. (*32*).

[c] Irrespective of stereospecific resonance assignments, low-field and high-field resonances are signified by *x* and *y*, respectively. Mutually active and passive $^3J(H^\alpha, H^\beta)$ coupling constants were soft-constrained and fixed, respectively, using values and standard deviations from Refs. (*26, 42*).

picted in Fig. 3 where two large couplings $^1J(C^\alpha, C')$ and $^1J(C^\alpha, C^\beta)$ are exploited in an E.COSY fashion (*41*) for separating, along $\omega_1$, the four multiplet contributions associated with the four states $|\alpha\alpha\rangle$, $|\alpha\beta\rangle$, $|\beta,\alpha\rangle$, and $|\beta\beta\rangle$ of the two passive spins C′ and $C^\beta$. Usually, small $^3J(H^N, C')$ and $^3J(H^N, C^\beta)$ coupling constants are found in amino-acid spin systems because the associated torsion angle $\phi$ frequently adopts dihedral values between −180° and −60°, a range coinciding with the conformational states encountered in many known protein secondary-structure elements (*71*). Indeed, these coupling constants are typically smaller than 3 Hz in antamanide. A large $^3J(H^N, C')$ coupling of 8–9 Hz would indicate $\phi \approx 0°$, while the $^3J(H^N, C^\beta)$ coupling takes maximum values up to 6 Hz only if $\phi = +120°$ (*72*). These results give a first indication of the predominant orientations of the nonproline backbone torsions in antamanide. Note that residue pairs five positions apart in the cyclic sequence exhibit similar backbone-related coupling constants as expected from the pseudo $C_2$ symmetry of the molecule.

The splitting due to the $^3J(H^\beta, C')$ coupling is present in the $(C^\alpha, H^\beta)$ correlation signal, where $\omega_1$ separation of the E.COSY multiplet components is achieved by the large $^1J(C^\alpha, C')$ coupling. For each of the phenylalanine residues, Phe[5], Phe[6], Phe[9], and Phe[10], the heteronuclear coupling constants $^3J(H^{\beta x}, C')$ and $^3J(H^{\beta y}, C')$ were determined from the respective $(C^\alpha, H^{\beta x})$ and $(C^\alpha, H^{\beta y})$ multiplets shown in Fig. 4. The multiplets exhibit prominent $^1J(H^\beta, C^\beta)$ splittings along $\omega_2$, and overlap and strong-coupling effects can be recognized. The $(C^\alpha, H^{\beta 3})$ multiplets of Phe[9] and Phe[10] remain below the minimum plot level because of weak magnetization transfer via unfavorably small homonuclear $^3J(H^\alpha, H^{\beta 3})$ couplings (*42*).

Likewise, the respective splitting due to the $^3J(H^\alpha, C^\gamma)$ coupling is present in the $(C^\beta, H^\alpha)$ correlation multiplet, where again the large $^1J(C^\alpha, C^\beta)$ coupling is exploited for separating the multiplet contributions along $\omega_1$. The multiplet also exhibits a prominent $^1J(H^\alpha, C^\alpha)$ splitting along $\omega_2$ because of the presence of the $^{13}C$ isotope attached to the observed nucleus $H^\alpha$. Figure 5 shows the region of the four $(C^\beta, H^\alpha)$ multiplets observed for phenylalanine residues Phe[5], Phe[6], Phe[9], and Phe[10] in antamanide. In agreement with the qualitatively known staggered orientations of the Phe[9], and Phe[10] side chains (*25*), small $^3J(H^\alpha, C^\gamma)$ coupling constants were found from the analysis. The largest value is found for Phe[6]; however, the magnitude is unlikely to represent a fixed orientation of the $H^\alpha-C^\alpha-C^\beta-C^\gamma$ fragment, neither *trans*-periplanar nor *gauche*-synclinal. The dihedral-angle geometries will be discussed in detail in the paper following.

In a similar manner, the corresponding $(C^\alpha, H^\beta)$ and $(C^\beta, H^\alpha)$ multiplets of Val[1] shown in Fig. 2 were analyzed. This involved considering a different substitution pattern at the $C^\beta$ site compared to that in phenylalanine topology. The resulting values for the conformationally relevant coupling constants, $^3J(H^\beta, C')$, $^3J(H^\alpha, C^{\gamma x})$, and $^3J(H^\alpha, C^{\gamma y})$, were found to be 2.59 ± 0.46, 3.02 ± 0.55, and 3.37 ± 0.57 Hz, respectively. The unique valine $^3J(H^\alpha, H^\beta)$ coupling constant of 6.55 ± 0.11 Hz was obtained from simulation of the $(C^\alpha, H^N)$ multiplet depicted in Fig. 3. The coupling constants $^3J(H^\alpha, H^\beta)$ and $^3J(H^\beta, C')$ in Ala[4] are conformationally averaged due to rapid methyl-group rotation, with values of 6.72 ± 0.03 and 4.34 ± 0.02 Hz, respectively, as evaluated from the $(C^\alpha, H^N)$ multiplet shown in Fig. 3 and from the $(C^\alpha, H^\beta)$ multiplet (not shown). Determination of $\chi_1$ in alanine is not important because the $H^\beta$ protons are equivalent.

Antamanide is known to undergo various backbone and side-chain conformational interconversions in the regime of rapid exchange, thus leading to averaged NMR parameters. The available extended set of high-precision $^3J$ coupling constants will be used as the experimental basis for the detailed determination of dihedral-angle values in antamanide (*73*).

*Other Spin-System Parameters in Antamanide*

Although the present work was aimed at determining the heteronuclear three-bond coupling constants, many other pa-

rameters and their standard deviations were provided by the iterative nonlinear-least-squares analysis of the 2D heteronuclear relayed E.COSY multiplets. Some of these experimental antamanide spin-system parameters are of potential utility for structure determination. Of particular interest are the apparent $H^N$ resonance linewidths. The ($C^\alpha$, $H^N$) multiplet simulations (Fig. 3) indicate a narrow range of values between 3.67 and 4.07 Hz for $Ala^4$, $Phe^5$, $Phe^9$, and $Phe^{10}$, while those in $Val^1$ and $Phe^6$ amount to 11.98 and 14.89 Hz, respectively. These results are in perfect agreement with the exchange of the hydrogen-bonding pattern in the antamanide backbone as postulated on the basis of rotating-frame relaxation studies (*30, 32*).

## DISCUSSION

Three-bond coupling constants are suitable measures of local conformation and thus yield information complementary to NOE effects, which help to determine the overall polypeptide fold. Conformational interconversion appears as an inherent property of peptide structure, and straightforward interpretation of *J*-coupling information with respect to geometry might be impeded by internal flexibility. The fact that a possibly very complex ensemble of conformations is characterized on the basis of only a few coupling constants may lead to ambiguous results. A reliable study of molecular conformational properties on the exclusive basis of spin–spin coupling constants therefore requires the determination of as many values as possible and, in addition, calls for utmost accuracy and precision of the reference $^3J$ values. Structure determination depends not only on the accuracy of the extracted coupling constants but also on the reliability of the Karplus parameters, as has recently been demonstrated (*53*). In the present work, particular emphasis was put on extracting accurate $^3J$ coupling constants for use in molecular structure refinement in the presence of conformational equilibria.

The $^3J$ coupling constants obtained from two-dimensional lineshape simulation of heteronuclear relayed E.COSY multiplets may be compared with previous results obtained by other evaluation methods. Preliminary coupling constants in Ref. (*32*) were obtained by an ad hoc procedure, i.e., simply from the differences between the center-of-gravity coordinates of the respective E.COSY multiplet components. Confidence intervals were only qualitatively estimated. Recent values in Ref. (*46*) were obtained by computer-assisted alignment of one-dimensional multiplet traces, an improved strategy capable of providing quantitative error estimates. However, both center-of-gravity determination and 1D trace alignment disregard artifacts from overlap of multiplet lines. The present 2D multiplet simulations include effects arising from overlap and from $C_2$ rotation symmetry. Confidence intervals were derived taking spin-system parameter covariance into account.

In the recent analysis (*46*) of ($C^\alpha$, $H^N$) patterns of $Ala^4$ and $Phe^9$ (Fig. 3), internal overlap of the central multiplet components caused major difficulties in obtaining appropriate 1D sections. Such systematic error was avoided in the present work by 2D multiplet simulation which yields improved coupling constants. However, the coupling constants $^3J(H^N, C')$ and $^3J(H^N, C^\beta)$ extracted from ($C^\alpha$, $H^N$) multiplets of $Val^1$, $Phe^5$, $Phe^6$, and $Phe^{10}$ agree within the experimental precision, irrespective of the evaluation method used. Symmetry effects were responsible for the slightly smaller values (0.01–0.11 Hz) determined with 1D trace projection methods.

Prominent examples of mutually overlapping patterns are ($C^\beta$, $H^\alpha$) multiplets of residues $Phe^5$ and $Phe^{10}$ depicted in Fig. 4 and ($C^\alpha$, $H^\beta$) multiplets of residues $Phe^5$ and $Phe^9$ in Fig. 5. Compared to 1D evaluation, the experimental uncertainty is expected to decrease in the 2D analysis as a consequence of the larger number of reference values bearing redundant information. Indeed, the standard deviations of the respective $^3J(H^\alpha, C^\gamma)$ and $^3J(C', H^\beta)$ coupling constants determined with 2D multiplet simulation are considerably smaller (0.1–0.2 Hz) than those in previous evaluations (0.6–0.8 Hz) and are similar to those obtained from isolated multiplets. It should be stressed that zero filling during spectrum processing to improve resolution does not increase the information content of the spectrum.

Even in the favorable case of isolated multiplet components, such as the $Val^1$ correlation patterns shown in Fig. 2, two-dimensional spectrum analysis is recommended. The unique valine $^3J(H^\beta, C')$ coupling constant of 2.59 Hz, found from two-dimensional ($C^\alpha$, $H^\beta$) multiplet reconstruction, is significantly larger than the value of 1.74 Hz found with 1D trace-alignment methods (*46*). Complete multiplet simulation is also justified, if not indispensable, for evaluating the $Val^1$ ($C^\beta$, $H^\alpha$) multiplet. Valine possesses two methyl groups in the positions $C^{\gamma 1}$ and $C^{\gamma 2}$ whose $^{13}C$ spins couple simultaneously to the $H^\alpha$ proton. The similar one-bond couplings, $^1J(C^\beta, C^{\gamma x})$ and $^1J(C^\beta, C^{\gamma y})$, cause overlap of the central splitting components along the $\omega_1$ dimension of the multiplet, thereby preventing appropriate sections from being extracted. As a consequence, trace-projection methods failed to resolve the individual contributions from the coupling constants $^3J(H^\alpha, C^{\gamma x})$ and $^3J(H^\alpha, C^{\gamma y})$. Without taking recourse to further experiments, numerical 2D multiplet synthesis gave the desired quantities with values of 3.02 and 3.37 Hz, respectively, while trace alignment allowed at most the sum of the two $^3J(H^\alpha, C^\gamma)$ coupling constants to be determined (*46*).

The convergence of the multiplet fit was acceptable if the residual $\epsilon^2_{\min}$ approached the number of data points *n*. From inspection of the variance–covariance matrix obtained during error analysis, it was found that the increased spectral resolution in the detection dimension $\omega_2$ compared to the dimension $\omega_1$ (see the legend to Fig. 2) resulted in generally tighter confidence intervals for parameters associated with $\omega_2$ than for those associated with $\omega_1$. For example, the standard

deviations of the positions $\nu_1$ and $\nu_2$ were typically 0.3 and 0.1 Hz, respectively. Multiplet positions generally showed negligible cross correlation with other fit parameters, while moderate cross correlation was observed within each pair of coupling parameters associated with a particular E.COSY tilt, including the desired three-bond coupling constants. As expected, the parameter covariance was largest within the set including amplitude, linewidth, and active COSY-type transfer couplings. Typically, the amplitude-scaling factors exhibited error margins of approximately 5%, while the precision of the linewidth and coupling parameters was usually a few tenths of a hertz. These findings agree with prior experience (*50*).

The relation between the error margins and the signal-to-noise (*S*/*N*) ratio is as intuitively expected. Major determinants of *S*/*N* are the active COSY-transfer coupling and the number of multiplet splittings due to passively coupled nuclei. Highest precision was found for $S/N \approx 20-80$, as shown for example by the ($C^{\alpha}$, $H^{N}$) multiplets depicted in Fig. 3, with standard deviations for $J(H^{N}, C')$ and $J(H^{N}, C^{\beta})$ ranging from 0.06 to 0.23 Hz. Intermediate *S*/*N* on the order of 10–20, as exemplified by the valine patterns in Fig. 2, led to elevated error margins in the range of 0.30–0.40 Hz. For *S*/*N* below 10, as in the invisible ($C^{\alpha}$, $H^{\beta}$) multiplets in Fig. 4, the confidence intervals are correspondingly larger than 1 Hz.

It should be pointed out that isotopic dilution may give rise to superimposed multiplet contributions that potentially affect the optimized parameter set. However, such artifact multiplets are expected to exhibit small intensities below the noise level, since the $^{13}C$ enrichment level is 98.6% in the present case (*46*). Numerically, the different splitting patterns of these artifact multiplets would assist in distinguishing the unwanted contributions. Serious perturbation of the fit, however, is expected if isotopic depletion is significant. This would require a weighted superposition of multiple patterns, in analogy to the treatment of the flip-angle dependence of E.COSY splittings (Eq. [3]). In contrast to isotope effects, overlapping multiplets of similar intensity, such as those shown in Figs. 4 and 5 represent by far the greater challenge and, in fact, have been treated satisfactorily. In a related project (*61*), 2D simulations have proven to be effective, even in the presence of significant $t_1$ noise.

## CONCLUSIONS

Numerical 2D NMR multiplet simulation was established as a tool for extracting high-precision $^{3}J$ coupling constants for molecular-geometry analysis. The method can be applied to complicated spin–spin coupling topologies such as those encountered in fully isotope-enriched biomolecules. The feasibility of exhaustive spectrum analysis has been demonstrated for the sample peptide antamanide. The coupling constants in the peptide were extracted with accuracy, and reliability significantly improved compared to previous results. The procedures are not restricted to small peptides, but may also be applied to larger molecules such as proteins, where linewidths are usually larger than *J* splittings.

## ACKNOWLEDGMENTS

The author thanks Saburo Aimoto and Masatsune Kainosho for the sample of $^{13}C$-labeled antamanide. Richard R. Ernst and co-workers are thanked for many stimulating discussions. Instrument time on a Bruker AMX-500 spectrometer was kindly provided by Spectrospin AG, Fällanden, Switzerland. This research has been supported by grants from the Deutsche Forschungsgemeinschaft (Schm 854/1-1) and by the Swiss National Science Foundation.

## REFERENCES

1. K. Wüthrich, ''NMR of Proteins and Nucleic Acids,'' Wiley, New York, 1986.
2. R. R. Ernst, G. Bodenhausen, and A. Wokaun, ''Principles of Nuclear Magnetic Resonance in One and Two Dimensions,'' Clarendon Press, Oxford, 1987.
3. N. J. Oppenheimer, and T. L. James (Eds.), ''Nuclear Magnetic Resonance. Part A: Spectral Techniques and Dynamics; Part B: Structure and Mechanism,'' Methods in Enzymology, Vols. 176/177, Academic Press, San Diego, 1989.
4. A. Bax, *Annu. Rev. Biochem.* **58,** 223 (1989).
5. G. Wagner, *Prog. NMR Spectrosc.* **22,** 101 (1990).
6. G. C. K. Roberts (Ed.), ''NMR of Macromolecules: A Practical Approach,'' Oxford Univ. Press, Oxford, 1993.
7. D. Neuhaus and M. Williamson, ''The Nuclear Overhauser Effect in Structural and Conformational Analysis,'' VCH, New York, 1989.
8. O. Jardetzky, *Biochem. Biophys. Acta* **621,** 227 (1980).
9. J. C. Hoch, *in* ''Computational Aspects of the Study of Biological Macromolecules by Nuclear Magnetic Resonance Spectroscopy'' (J. C. Hoch, F. M. Poulsen, and C. Redfield, Eds.), Plenum Press, New York, 1991.
10. D. Zhao and O. Jardetzky, *J. Mol. Biol.* **239,** 601 (1994).
11. A. Bax and D. G. Davis, *J. Magn. Reson.* **63,** 355 (1985).
12. D. A. Case, H. J. Dyson, and P. Wright, *Meth. Enzymol.* **239,** 392 (1994).
13. C. Biamonti, C. B. Rios, B. A. Lyons, and G. T. Montelione, *Adv. Biophys. Chem.* **4,** 51 (1994).
14. M. Eberstadt, G. Gemmecker, D. M. Mierke, and H. Kessler, *Angew. Chem.* **107,** 1813 (1995); *Angew. Chem. Int. Ed.* **34,** 1671 (1995).
15. M. Karplus, *J. Chem. Phys.* **30,** 11 (1959).
16. M. Karplus, *J. Am. Chem. Soc.* **85,** 2870 (1963).
17. T. Wieland and H. Faulstich, *Crit. Rev. Biochem.* **5,** 185 (1978).
18. G. Raymond, D. Potreau, C. Cognard, W. Jahn, and T. Wieland, *Eur. J. Pharmacol.* **138,** 21 (1987).
19. H. Kataoka, T. Katagi, H. Yajima, and A. Otaka, *Chem. Pharm. Bull.* **36,** 3196 (1988).
20. K. Münter, D. Mayer, and H. Faulstich, *Toxic. in Vitro* **4,** 201 (1989).
21. R. J. Korthuis, D. L. Carden, P. R. Kvietys, D. Shepro, and J. Fuseler, *J. Appl. Physiol.* **71,** 1261 (1991).
22. R. Welbourn, G. Goldman, L. Kobzik, C. R. Valeri, H. B. Hechtman, and D. Shepro, *J. Appl. Physiol.* **70,** 1364 (1991).
23. I. L. Karle, T. Wieland, D. Schermer, and H. C. J. Ottenheym, *Proc. Natl. Acad. Sci. USA* **76,** 1532 (1979).
24. I. L. Karle, *J. Am. Chem. Soc.* **96,** 4000 (1974).

25. H. Kessler, C. Griesinger, and K. Wagner, *J. Am. Chem. Soc.* **109,** 6927 (1987).
26. H. Kessler, A. Müller, and K.-H. Pook, *Liebigs Ann. Chem.* 903 (1989).
27. H. Kessler, J. W. Bats, J. Lautz, and A. Müller, *Liebigs Ann. Chem.* 913 (1989).
28. H. Kessler, C. Griesinger, J. Lautz, A. Müller, W. F. van Gunsteren, and H. J. C. Berendsen, *J. Am. Chem. Soc.* **110,** 3393 (1988).
29. R. Brüschweiler, M. Blackledge, and R. R. Ernst, *J. Biomol. NMR* **1,** 3 (1991).
30. R. R. Ernst, M. Blackledge, S. Boentges, J. Briand, R. Brüschweiler, M. Ernst, C. Griesinger, Z. L. Mádi, T. Schulte-Herbrüggen, and O. W. Sørensen, *in* ''Proteins: Structure, Dynamics and Design'' (V. Renugopalakrishnan, P. R. Carey, I. C. P. Smith, S. G. Huang, and A. C. Storer, Eds.), p. 11, ESCOM, Leiden, 1991.
31. R. Brüschweiler, B. Roux, M. Blackledge, C. Griesinger, M. Karplus, and R. R. Ernst, *J. Am. Chem. Soc.* **114,** 2289 (1992).
32. M. J. Blackledge, R. Brüschweiler, C. Griesinger, J. M. Schmidt, Ping Xu, and R. R. Ernst, *Biochemistry* **32,** 10960 (1993).
33. M. Ernst and R. R. Ernst, *J. Magn. Reson. A* **110,** 202 (1994).
34. T. Bremi, M. Ernst, and R. R. Ernst, *J. Phys. Chem.* **98,** 9322 (1994).
35. T. C. Beutler, T. Bremi, R. R. Ernst, and W. F. van Gunsteren, *J. Phys. Chem.* **100,** 2637 (1996).
36. Z. L. Mádi, C. Griesinger, and R. R. Ernst, *J. Am. Chem. Soc.* **112,** 2908 (1990).
37. R. M. Brunne, W. F. van Gunsteren, R. Brüschweiler, and R. R. Ernst, *J. Am. Chem. Soc.* **115,** 4764 (1993).
38. J. M. Schmidt, R. Brüschweiler, R. R. Ernst, R. L. Dunbrack Jr., D. Joseph, and M. Karplus, *J. Am. Chem. Soc.* **115,** 8747 (1993).
39. H. Kessler, A. Müller, and H. Oschkinat, *Magn. Reson. Chem.* **23,** 844 (1985).
40. C. Griesinger, O. W. Sørensen, and R. R. Ernst, *J. Am. Chem. Soc.* **107,** 6394 (1985).
41. C. Griesinger, O. W. Sørensen, and R. R. Ernst, *J. Chem. Phys.* **85,** 6837 (1986).
42. C. Griesinger, O. W. Sørensen, and R. R. Ernst, *J. Magn. Reson.* **75,** 474 (1987).
43. B. U. Meier, Z. L. Mádi, and R. R. Ernst, *J. Magn. Reson.* **74,** 565 (1987).
44. B. U. Meier and R. R. Ernst, *J. Magn. Reson.* **79,** 540 (1988).
45. Z. L. Mádi and R. R. Ernst, *J. Magn. Reson.* **79,** 513 (1988).
46. J. M. Schmidt, R. R. Ernst, S. Aimoto, and M. Kainosho, *J. Biomol. NMR* **6,** 95 (1995).
47. L. Müller, *J. Am. Chem. Soc.* **101,** 4481 (1979).
48. A. Bax, R. H. Griffey, and B. L. Hawkins, *J. Magn. Reson.* **55,** 301 (1983).
49. M. H. Frey, G. Wagner, M. Vašak, O. W. Sørensen, D. Neuhaus, E. Wörgötter, J. H. R. Kägi, R. R. Ernst, and K. Wüthrich, *J. Am. Chem. Soc.* **107,** 6847 (1985).
50. J. M. Schmidt, O. W. Sørensen, and R. R. Ernst, *J. Magn. Reson. A* **109,** 80 (1994).
51. H. Schwalbe, A. Rexroth, U. Eggenberger, T. Geppert, and C. Griesinger, *J. Am. Chem. Soc.* **115,** 7878 (1993).
52. S. Boentges, B. U. Meier, C. Griesinger, and R. R. Ernst, *J. Magn. Reson.* **85,** 337 (1989).
53. Y. Karimi-Nejad, J. M. Schmidt, H. Rüterjans, H. Schwalbe, and C. Griesinger, *Biochemistry* **33,** 5481 (1994).
54. W. Studer, *J. Magn. Reson.* **77,** 424 (1988).
55. S. A. Smith, T. O. Levante, B. H. Meier, and R. R. Ernst, *J. Magn. Reson. A* **106,** 75 (1994).
56. O. W. Sørensen, G. W. Eich, M. H. Levitt, G. Bodenhausen, and R. R. Ernst, *Prog. NMR Spectrosc.* **16,** 163 (1983).
57. J. A. Nelder and R. Mead, *Computer J.* **7,** 308 (1965).
58. M. A. Thomas, and A. Kumar, *J. Magn. Reson.* **61,** 540 (1985).
59. J. W. Emsley, J. Feeney, and L. H. Sutcliffe, ''High Resolution Nuclear Magnetic Resonance Spectroscopy,'' Vols. 1 and 2, Pergamon, New York, 1965.
60. D. Graveron-Demilly, A. Diop, and B. Fenet, *J. Magn. Reson. A* **101,** 233 (1993).
61. J. M. Schmidt, F. Löhr, and H. Rüterjans, *J. Biomol. NMR* **7,** 142 (1996).
62. C. G. Broydon, *J. Inst. Math. Appl.* **6,** 76 (1970).
63. R. Fletcher, *Computer J.* **13,** 317 (1970).
64. D. Goldfarb, *Math. Comput.* **24,** 23 (1970).
65. D. F. Shanno, *Math. Comput.* **24,** 647 (1970).
66. A. A. Clifford, ''Multivariate Error Analysis,'' Applied Science, London, 1973.
67. M. Merrington and C. M. Thompson, *Biometrika* **33,** 73 (1948).
68. R. R. Sokal and F. J. Rohlf, ''Biometry—Statistical Tables,'' 2nd ed., W. H. Freeman, New York, 1981.
69. W. H. Press, B. P. Flannery, S. A. Teukolsky, and W. T. Vetterling, ''Numerical Recipes,'' Cambridge Univ. Press, Cambridge, 1989.
70. M. L. Johnson, *Biophys. J.* **44,** 101 (1983).
71. T. E. Creighton, ''Proteins: Structures and Molecular Properties,'' 2nd ed., W. H. Freeman, New York, 1993.
72. V. F. Bystrov, *Prog. NMR Spectrosc.* **10,** 41 (1976).
73. J. M. Schmidt, *J. Magn. Reson.* **124,** 310 (1997).